

REGISTRATION OF RENAL SPECT AND 2.5D US IMAGES

Francisco J. GALDAMES^{a,c}, Claudio A. PEREZ^{a,b}, Pablo A. ESTÉVEZ^{a,b}, Claudio M. HELD^a, Fabrice JAILLET^c, Gabriel LOBO^d, Gilda DONOSO^d, Claudia COLL^d

^aDepartment of Electrical Engineering, Universidad de Chile, Av. Tupper 2007, Santiago, Chile

^bAdvanced Mining Technology Center, Universidad de Chile, Av. Tupper 2007, Santiago, Chile

^cUniversité de Lyon, CNRS, Université Lyon 1, LIRIS, équipe SAARA, UMR5205, F-69622, France

^dMedicina Nuclear, Hospital San Juan de Dios, Santiago, Chile

Abstract

Image registration is the process of transforming different image data sets of an object into the same coordinate system. This is a relevant task in the field of medical imaging; one of its objectives is to combine information from different imaging modalities. The main goal of this study is the registration of renal SPECT (Single Photon Emission Computerized Tomography) images and a sparse set of ultrasound slices (2.5D US), combining functional and anatomical information. Registration is performed after kidney segmentation in both image types. The SPECT segmentation is achieved using a deformable model based on a simplex mesh. The 2.5D US image segmentation is carried out in each of the 2D slices employing a deformable contour and Gabor filters to capture multi-scale image features. Moreover, a renal medulla detection method was developed to improve the US segmentation. A nonlinear optimization algorithm is used for the registration. In this process, movements caused by patient breathing during US image acquisition are also corrected. Only a few reports describe registration between SPECT images and a sparse set of US slices of the kidney, and they usually employ an optical localizer, unlike our method, that performs movement correction using information only from the SPECT and US images. Moreover, it does not require simultaneous acquisition of both image types. The registration method and both segmentations were evaluated separately. The SPECT segmentation was evaluated qualitatively by medical experts, obtaining a score of 5 over a scale from 1 to 5, where 5 represent a perfect segmentation. The 2.5D US segmentation was evaluated quantitatively, by comparing our method with an expert manual segmentation, and obtaining an average error of 3.3mm. The registration was evaluated quantitatively and qualitatively. Quantitatively the distance between the manual segmentation of the US images and the model extracted from the SPECT image was measured, obtaining an average distance of 1.07 pixels on 7 exams. The qualitative evaluation was carried out by a group of physicians who assessed the perceived clinical usefulness of the image registration, rating each registration on a scale from 1 to 5. The average score obtained was 4.1, i.e. relevantly useful for medical purposes.

Keywords: kidney, image registration, image segmentation, SPECT, US, ultrasound, renal medulla detection

1. Introduction

The use of medical imaging for diagnosis, treatment planning and evaluation is crucial in current clinical procedures. The data provided about the organs by images can be classified as functional or anatomical. One of the medical imaging modalities that provide 3D functional information is the SPECT (Single Photon Emission Computerized Tomography), which uses radioactive tracers, i.e., substances that are introduced into the body and tend to accumulate in specific organs, without modifying their normal function [1]. Particularly, applied to the kidney, the radiopharmaceuticals employed

in SPECT are absorbed by functioning tubular cells of the renal cortex, allowing to quantify the perfusion and renal functional mass. Moreover, this application can be used to detect cortical alterations related to urinary tract infections, and acute or chronic lesions in the renal cortex [2]. However, uncertainty in the anatomic definition of the SPECT image may limit its usefulness. Often, there is not enough anatomical detail to determine the exact position of a lesion or to compare the renal functional mass with the total organ size. A way to overcome this problem is to integrate SPECT images with anatomical images of the kidneys. One of the most used

images for this integration are the US (Ultrasound) images, because of their relatively low cost, innocuousness (no ionizing radiation) and easy acquisition [3]. Since the SPECT is a 3D image, it is more adequate to use US images with spatial information. A good option is to use 2D freehand US images with associated spatial coordinates (2.5D US). To integrate both, a registration between SPECT and US images is necessary.

Image registration is the process of transforming different images into the same coordinate system [4]. Images to be registered may be of the same modality (monomodal registration) or different modalities (multimodal registration). In multimodal registration, the data obtained from the same organ of a patient by different imaging modalities is transformed into a single coordinate space to compare or integrate. There are different approaches to carry out image registration. One option is to use *extrinsic methods* based on positioning a foreign object introduced into the image, such as a stereotactic frame [5], screw-mounted markers [6] or markers glued to the skin [7]. Although efficient, these are invasive approaches. Another possibility is to base the registration on a previous spatial calibration of the coordinate systems associated with the scanners [8]. To use this approach, the imaging systems must be in the same room and the patient must remain in the same position for both image acquisitions. Another alternative is to use *intrinsic methods*, i.e., register with the information contained in the images. Examples of this approach are methods based on features identified manually [9], statistical measures [10, 11] or image segmentation [12] or

In our literature review we found only a few papers on registration between SPECT images and a sparse set of US slices. In [13] they use a method based on MI (Mutual Information) for the registration of cardiac images. Particularly for kidney images, two studies use an optical localizer [14, 15].

However, there are other examples of image registration between a sparse set of 2D images and a 3D image, not necessarily a SPECT volume and a set of 2D US images. A study that uses US and CT (Computer Tomography) images of kidneys is described in [16], where the registration is carried out by minimizing a correlation ratio (CR) between the images pre-processed to remove noise and enhance edges. There are also registrations that use US and CT images in different organs, such as in [17], where images of head and neck are registered using a multi-component similarity measure involving weighted MI, intensities and edge maps. Another example using CT images is [18], in which US images of liver and kidney are registered with CT by

a method that simulates US images using the CT data, and then registers the US image applying a similarity measure between it and the simulation. A US simulation is also used in [19] for a biomechanically constrained registration of lumbar spine CT and US images. In [20] prostate phantom CT and US images are registered using an ICP (Iterative Closest Point) algorithm and a semi-manual urethral surface segmentation. Another study using prostate phantom CT and US images is [21], where the images are registered employing MI in a user-defined bounding box within the images. A study using a MI technique to register beating heart CT and 2D US images is [22]. Other studies have used MRI (Magnetic Resonance Imaging), such as [23] where US and MRI head images are registered using intensity and gradient information. 3D US and MRI images of the heart are registered in [24] using MI, normalized cross-correlation, and a threshold to emphasize the most apparent anatomical features. Also MRI and 3D US images are registered in [25], but using female pelvic floor images and manually identified points as fiducial marks. The vessels have also been used as references to registration. In [26], the vessels are segmented using Doppler images to register abdominal MRI and 3D US images. In [27] liver models from MRI and CT images are registered with US images using the center lines of vessels. The probability of existence of vessels has been used as reference in [28] to register US and MRI liver images, minimizing the cross-correlation of these probabilities between both images. In an extension of that work [29], the probability of presence of bone edges was used in a similar way to register US and CT cadaver images of femur and pelvis.

There are also publications on monomodal registration between US images, as in [30], where a correlation measure is used together with a mechanical elastic regularization on preoperative 3D US and intraoperative freehand 2D US images of prostate, or in [31], where MI is used on 3D US cardiac images. A study [32] shows registration between 3D statistical shape models and 2D US images of cadavers, by minimizing the distance between the model surfaces and US-derived bone surface points. In our literature review, we found that most studies use MRI or CT images for image registration with US slices. The lack of structural information in SPECT images together with the intrinsic low quality of US images are the main problems inherent to SPECT-US registration. The aim of our work is to overcome these registration problems using only information contained in the images (intrinsic methods).

Our method is based on the segmentation of both SPECT and US images, as the first step. Then this

segmentation is used to drive the registration. Patient movement during kidney image acquisition, caused primarily by breathing, is a relevant problem for the registration task [16]. Breathing movement has been quantified to be up to 40mm [33], causing kidneys to appear in different positions along the acquisition of the 2.5D US slices. These position inconsistencies also happen in the image acquisition of other organs located in the abdomen. For example, the same problem is addressed in [34] for liver images, using a single-parameter respiratory motion model for the registration between preoperative MRI and intraoperative US images. We tackle this problem using specific registrations to locally correct the position of each slice of the 2.5D US image. First, the 2.5D US image is registered using a similarity transformation over the entire image, and when the slices are close enough to their correct registered positions, local registrations are used to correct each slice individually. Subsequently, the global registration can be improved and the specific position of each slice can be re-corrected again.

2. Methods

The renal SPECT and US images we used in this work are normally employed for medical diagnosis after being acquired separately. Therefore, our registration is carried out after both images are acquired. This is different from related works found in the literature [14, 15], which use an optical localizer to perform an online registration (we used a localizer but only during the image acquisition to know the relative spatial position among the 2D US images that constitute the 2.5D US image). Our method involves segmenting the 2.5D US and SPECT images first, and then carry out the registration by finding the transformation that matches the edges found in both segmentations. Fig. 1 shows a flow diagram of the proposal registration process.

To segment the SPECT images we use a deformable model [35]. Two types of forces to control the model, based on gradient and on voxels intensity respectively, were tested to establish which of these two segmentation types would be better for registration. To segment the US images we use a deformable contour method. The deformable contours are controlled by a field of forces derived from multi-scale image features obtained by Gabor filters. To obtain a smooth field of forces without undesired local minima, the Gradient Vector Flow (GVF) algorithm [36] was used. Active contours and the GVF algorithm, have been successfully applied in other works of US image segmentation as [37, 38]. Additionally, we developed a method to detect the renal

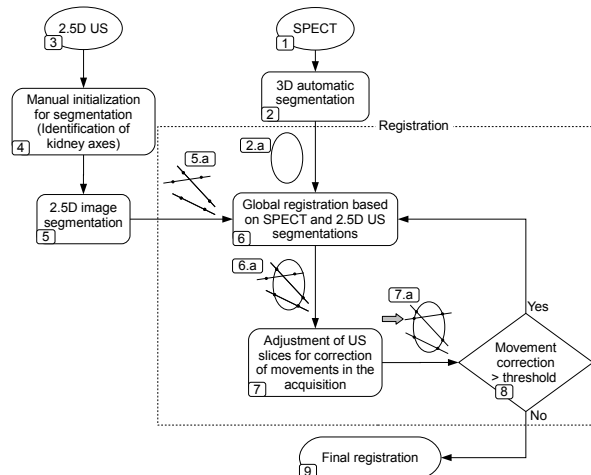


Figure 1: Flow diagram of our image registration algorithm. 1) Acquisition of SPECT image (sec. 2.1). 2) Automatic segmentation of SPECT image based on deformable models (sec. 2.1.1). 2.a) The result of the segmentation is a mesh that represents the kidney borders. 3) Acquisition of 2.5D US image (sec. 2.2). 4) Manual initialization of 2.5D US image segmentation, based on fitting an ellipsoid to the kidney by the identification of the kidney main axes (sec. 2.2.1). 5) 2.5D US image segmentation based on deformable models and Gabor filters (sec. 2.2.1). 5.a) The segmentation gives a set of contour points (dark dots) for every slice (dark lines) of the 2.5D image. 6) Global registration using the segmentation of both images. The registration deforms the 2.5D image using a similarity transformation over the whole image (sec. 2.3). 6.a) After registration, the edges found in both images are closer, but there are still slices out of registered due to inconsistencies in the 2.5D US image caused by patient motion during acquisition. 7) A local registration is performed to correct the out of registered US slices (sec. 2.3). 7.a) After the local registration, the misregistered slices are corrected. 8) If the movement of the slices in the local registration was over a threshold, another global registration is performed, if not, the registration is finished. 9) After the process, both images are registered and the movements during the 2.5 US image acquisition are corrected.

medulla. This detection was needed to avoid forces created at the medulla borders from interfering in the segmentation of the outer edges of the kidney.

2.1. The SPECT Modality

First we explain the kidneys segmentation in the SPECT image. The radioactive isotope used in these images is transported by the blood flow and fixed in the renal cortex, thus exhibiting kidneys perfusion and function. The images are acquired using a gamma camera that captures projections of the radiation at different angles. Next, an algorithm of tomographic reconstruction is used to obtain the 3D image with these projections.

2.1.1. SPECT Segmentation

The kidneys on the SPECT image were segmented using a deformable model method because of its robustness and high noise immunity [35]. A simplex mesh [39] iteratively adjusted to the shape of the kidney was used for the segmentation. The simplex meshes have been successfully applied elsewhere, e.g., to the segmentation of cardiac SPECT images [40] and in our preliminary work on renal segmentation [41] and registration [42].

First, we introduce a general description of the simplex meshes.

A k -simplex is the convex hull of $k+1$ independent points e.g. a segment is a 1-simplex, a triangle is a 2-simplex and a tetrahedron is a 3-simplex. By definition a k -simplex mesh has a $(k+1)$ -simplex in each vertex. For example, a 1-simplex mesh is a contour in which each vertex and its two neighbors define a triangle. This property defines the connectivity of the mesh, i.e. the vertices of a k -simplex mesh have $k+1$ neighbors. The type of objects that these meshes can represent depends on this connectivity e.g. a k -simplex with $k=1$ can represent a curve, $k=2$ a surface, $k=3$ a volume. Since we want to segment the kidney surface, we use 2-simplex meshes. Each vertex of these meshes has three neighbors, and these four points define a tetrahedron (Fig. 2(b)): $P_i, P_{N1(i)}, P_{N2(i)}, P_{N3(i)}$. An interesting feature of 2-simplex meshes is that they are topologically dual of triangulations (meshes of triangles); this allows to obtain a 2-simplex mesh by applying a dual operation to a triangulation, and vice versa (Fig. 2(a)). This property is useful because it is more convenient to represent a surface with a triangulation for some tasks, e.g. rendering, calculation of intersections or the construction of volumetric meshes. From now on we will refer to 2-simplex meshes simply as simplex meshes.

Now, we give a brief explanation of the simplex mesh local geometry.

As mentioned above, each vertex of a simplex mesh positioned at P_i has three neighbors, positioned at $P_{N1(i)}, P_{N2(i)}, P_{N3(i)}$. The vertex and its neighbors form a tetrahedron (see Fig. 2(b)). We can calculate the sphere with center O_i and radius R_i defined by these four points (the circumscribed sphere of the tetrahedron), and the circle of center C_i and radius r_i defined by the three neighbors. The three neighbors also define a plane with normal \vec{N}_i , which includes the circle with center C_i . With these geometric entities, the simplex angle ρ_i can

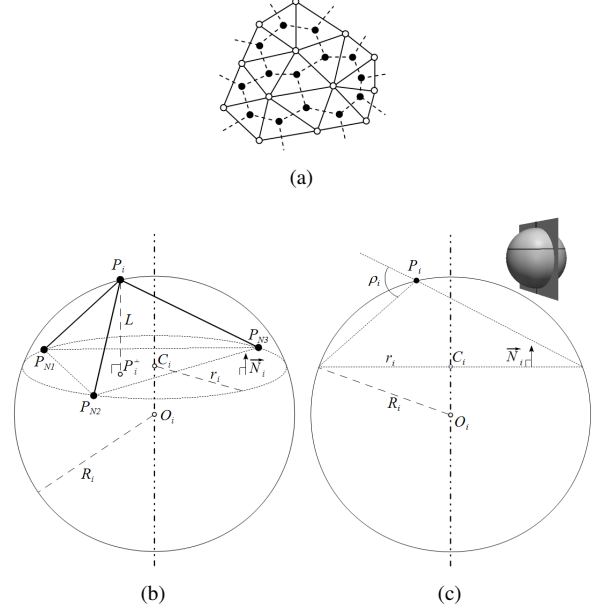


Figure 2: (a) 2-simplex mesh (dark dots) and its dual triangulation (white dots). (b) Local geometry of a 2-simplex mesh. The tetrahedron formed by a vertex P_i and its 3 neighbors $P_{N1(i)}, P_{N2(i)}, P_{N3(i)}$ is shown. These four points (vertex P_i and its neighbors) define the circumscribed sphere of the tetrahedron, with center O_i and radius R_i . Also, the three neighbors define the circle of center C_i and radius r_i . (c) Simplex angle ρ_i shown in a cut passing through the vertex P_i and the axis of the sphere $O_i C_i$.

be defined (see Fig. 2(c)):

$$\begin{aligned} \rho_i &\in [-\pi, \pi] \\ \sin(\rho_i) &= \frac{r_i}{R_i} \operatorname{sgn}(\overrightarrow{P_i P_{N1(i)}} \cdot \vec{N}_i) \\ \text{or} \\ \cos(\rho_i) &= \frac{\|O_i C_i\|}{R_i} \operatorname{sgn}(\overrightarrow{O_i C_i} \cdot \vec{N}_i) \end{aligned} \quad (1)$$

where sgn is the *sign* function and (\cdot) is the dot product. So, the simplex angle ρ_i is defined in every vertex P_i by means of its neighbors $P_{N1(i)}, P_{N2(i)}, P_{N3(i)}$, and it does not depend on the position of the neighbors within the circle they define. The simplex angle and the height L (Fig. 2(b)) of P_i over the plane defined by its neighbors are related by:

$$\begin{aligned} L(r_i, d_i, \rho_i) &= \frac{(r_i^2 - d_i^2) \tan(\rho_i)}{\chi \sqrt{r_i^2 + (r_i^2 - d_i^2) \tan^2(\rho_i) + r_i}} \\ \chi &= \begin{cases} 1 & \text{if } |\rho_i| < \pi/2 \\ -1 & \text{if } |\rho_i| > \pi/2 \end{cases} \end{aligned} \quad (2)$$

where $d_i = \|C_i P_i^\perp\|$, and P_i^\perp is the projection of P_i over

the plane defined by its neighbors. Since the simplex angle is scale-invariant, it can be considered a local and scale-invariant measure of the height L of P_i over the plane defined by its neighbors. Moreover, the simplex angle is related with the surface curvature at P_i . We can approximate the curvature at P_i by the curvature of the sphere that best fit the surface in a neighborhood around P_i . If we consider the neighbors $P_{N1(i)}, P_{N2(i)}, P_{N3(i)}$ of P_i , this sphere is the circumscribed sphere of the tetrahedron formed by the four points (Fig. 2(b)), and its mean curvature is $H_i = 1/R_i$. This mean curvature at point P_i can be expressed in terms of the simplex angle [39] using the equation (1): $H_i = \frac{\sin(\rho_i)}{r_i}$.

Other important geometric entities of the simplex meshes are the metric parameters $\varepsilon_{1i}, \varepsilon_{2i}, \varepsilon_{3i}$. These parameters are the barycentric coordinates of the projection P_i^\perp of the vertex P_i on the triangle defined by its neighbors (Fig. 2(b)):

$$\begin{aligned} P_i^\perp &= \varepsilon_{1i}P_{N1(i)} + \varepsilon_{2i}P_{N2(i)} + \varepsilon_{3i}P_{N3(i)} \\ \varepsilon_{1i} + \varepsilon_{2i} + \varepsilon_{3i} &= 1 \end{aligned} \quad (3)$$

We know the position of a vertex projection on the plane defined by its neighbors by equation (3), and the height of the vertex over this plane by equation (2). Therefore, the metric parameters and the simplex angle completely determine the position of the vertex as follows:

$$P_i = \varepsilon_{1i}P_{N1(i)} + \varepsilon_{2i}P_{N2(i)} + \varepsilon_{3i}P_{N3(i)} + L(r_i, d_i, \rho_i)\vec{N}_i \quad (4)$$

The deformation of a simplex mesh can be controlled by internal and external forces. The external forces are computed from the image, and push the mesh to the desired borders; the internal forces are computed from the mesh, caring for a smooth deformation and keeping the mesh regularity.

Now, we describe how the mesh can be deformed. The dynamic of the model is controlled by means of a Newtonian law of motion:

$$m \frac{\partial^2 P_i}{\partial t^2} = -\gamma \frac{\partial P_i}{\partial t} + \vec{F}_{int_i} + \vec{F}_{ext_i}, \quad (5)$$

where m is the mass unit of a vertex (usually 1), γ is a damping factor, P_i is the position of vertex i , F_{int_i} represents the internal force at vertex i , and F_{ext_i} represent the the external force. Considering discrete time and using finite differences we obtain:

$$P_i^{t+1} = P_i^t + (1 - \gamma)(P_i^t - P_i^{t-1}) + \vec{F}_{int_i} + \vec{F}_{ext_i} \quad (6)$$

The internal force of a simplex mesh can be locally determined by the simplex angle ρ_i and the metric parameters $\varepsilon_{1i}, \varepsilon_{2i}, \varepsilon_{3i}$. The internal force is derived from

the minimization of a local energy $S_i = \frac{\lambda}{2} \overrightarrow{P_i P_i^*}^2$, where P_i^* is the position the vertex should have to comply with a desired simplex angle ρ_i^* and metric parameters $\varepsilon_{1i}^*, \varepsilon_{2i}^*, \varepsilon_{3i}^*$. In this way, the local curvature of the mesh may be controlled by the simplex angle, and the vertex position relative to its neighbors by the metric parameters. By minimizing the energy, the internal force is: $\vec{F}_{int_i} = \frac{\partial S_i}{\partial P_i} = \lambda \overrightarrow{P_i P_i^*}$. If we use equation (4) to express the vertex position, the internal force can be written as:

$$\begin{aligned} \vec{F}_{int_i} &= \lambda \left(\varepsilon_{1i}^* \overrightarrow{P_i P_{N1(i)}} + \varepsilon_{2i}^* \overrightarrow{P_i P_{N2(i)}} + \varepsilon_{3i}^* \overrightarrow{P_i P_{N3(i)}} \right. \\ &\quad \left. + L(r_i, d_i, \rho_i^*) \vec{N}_i \right) \end{aligned} \quad (7)$$

In our work ρ_i^* is defined by a mean curvature continuity constraint [39] computed over a neighborhood around each vertex, and the metric parameters are fixed to 1/3, to obtain a regular mesh.

To compute the external force F_{ext_i} in each vertex, a field of external forces \vec{v} is used. We tested two types of mesh deformations with different external force fields. The first type was based on the voxels intensity. The field of forces for this segmentation is defined by the potential $\mathcal{P} = -\|\nabla [G_\sigma * I_b]\|^2$ (normalized in [0,1]) that must be minimized in each vertex, where I_b is a binarized SPECT image of the kidneys and G_σ is a Gaussian function. Thus, in order to obtain forces that push the model to low-potential zones, the external force field is computed as: $\vec{v} = -\nabla \mathcal{P}$. The result of this segmentation is similar to an isosurface but smoothed because of the mesh internal forces. The second type of deformation was a gradient related segmentation that uses the GVF algorithm [36] to compute the field of forces. The GVF algorithm compute a field of forces using an edge map as input, preserving only the forces that point towards the main edges. To compute the edge map \mathcal{H} as high gradient zones, a Sobel filter was used:

$$\mathcal{H} = \sqrt{(I * S_x)^2 + (I * S_y)^2 + (I * S_z)^2} \quad (8)$$

where I is the SPECT image, and S_x, S_y, S_z are the components of a 3D sobel filter. This edge map was normalized in the interval [0,1] before being used in the GVF algorithm. In this way, the deformable model is pushed to higher gradient zones that correspond to edges in the image.

Only the projection of the external force on the unit vector normal to the mesh surface is considered in every vertex, since the tangent component affects only the parametrization of the surface but not its shape. Therefore the external force is:

$$\vec{F}_{ext_i} = \kappa \vec{N}_i \cdot \vec{v}_i, \quad (9)$$

where κ is the weight of the external force.

The initial mesh to segment each kidney is defined by an isosurface at 15% of the maximum value in the image, and computed by the “marching tetrahedra” algorithm [43]. This algorithm generates a triangulation from which we can directly calculate the dual simplex mesh. Equation (6) is used iteratively over the N_p points of the mesh, until the mean deformation of the mesh in one step $MD = \frac{1}{N_p} \sum_{i=1}^{N_p} \|P_i^{t+1} - P_i^t\|$ is smaller than a threshold. Fig. 3 shows a kidney segmentation by a simplex mesh deformed by forces derived from image gradient.

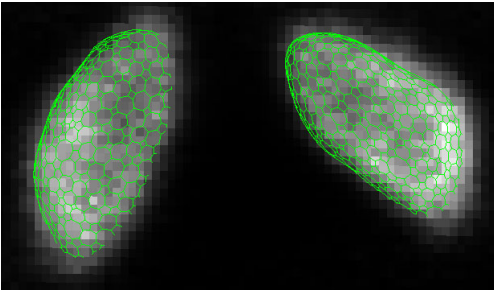


Figure 3: SPECT image segmented by a simplex mesh using deformable models

2.2. The 2.5D US modality

The US images were acquired using a localizer that tracked the positions of two rigid bodies, one fixed to the US probe and another fixed to the bed. The relative spatial location among the US slices can be known using a spatial transformation between the reference systems associated with the two rigid bodies (Fig. 4). The resulting image does not constitute a proper 3D reconstruction, because the arbitrary manual displacement of the US probe leads to 2D images located in different places and orientations. However, knowing the spatial location allows us to compensate for the lack of a full regular volume; this image is known as a 2.5D image. Every of the 2.5D US images used in this work was composed of approximately 400 2D US slices.

2.2.1. Segmentation of 2.5D US images

Unlike other medical imaging modalities, segmentation of US images is particularly difficult because the image quality is relatively low, with significant noise. Moreover, the kidney tissue boundary in US images is more difficult to localize than the edges of other organs; even for an expert the segmentation is not straightforward [44], and usually requires manual initialization. Our method uses manual initialization, which consists

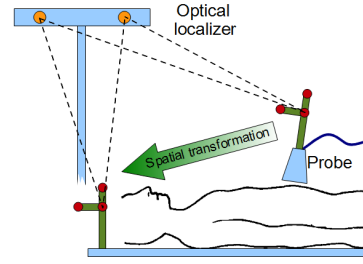


Figure 4: Spatial localization of the US slices that compose the 2.5D US image. An optical localizer tracks the position of two rigid bodies, one fixed to the bed and another fixed to the US probe. The relative spatial location among the slices can be obtained using a spatial transformation between the reference systems associated with the two rigid bodies.

in aligning the axes of an ellipsoid with the kidney position in a single 2D US slice (Fig. 5). After this initialization, an automated 2D segmentation is performed on each 2D image of the set that conforms the 2.5D US image, applying a deformable contour [44, 45] method and a set of Gabor filters [46, 47, 48, 49] to capture multi-scale image features.

The aim of our method is to find enough points in the US image to carry out the registration, rather than finding the whole kidney geometry.

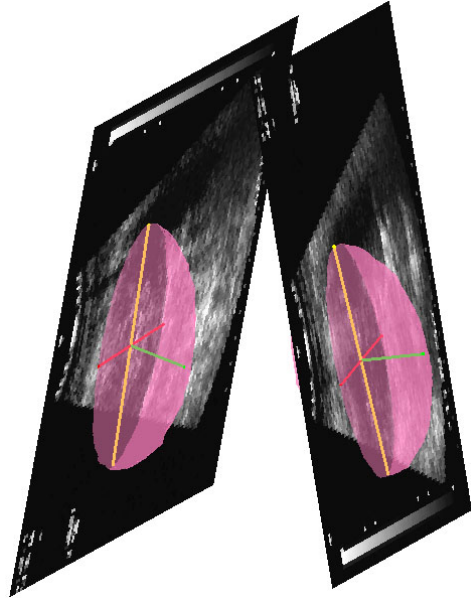


Figure 5: The initialization of the 2.5D US image segmentation of each kidney is based on the manual location of the axes of an ellipsoid in a single 2D US slice, so that they are aligned with the principal axes of the kidney in 3D.

Initialization. The manual initialization consists on fitting a 3D ellipsoid to the location of each kidney. To define the position of the ellipsoids, the user has to choose two 2D US images, one per kidney, and in each image to identify two kidney principal axes over three. The axes that must be identified are the longest axis, which are the axial axis, and one of the two smaller axes: the sagittal or the coronal. The third axis of the ellipsoid is calculated using the other two, it is orthogonal to them and has the same length as the identified small axis. Fig. 5 shows the two images and the kidney principal axes in 3D. A graphical interface is used to choose a central slice of each kidney and then locate two principal axes by moving, rotating and selecting the length of each axis, as shown in Fig. 6. The kidney shape is simplified as an ellipsoid (3D), and the intersections between this ellipsoid and the different planes of the US slices are used as the initial estimation of the kidney position in the 2D US images (Fig. 7).

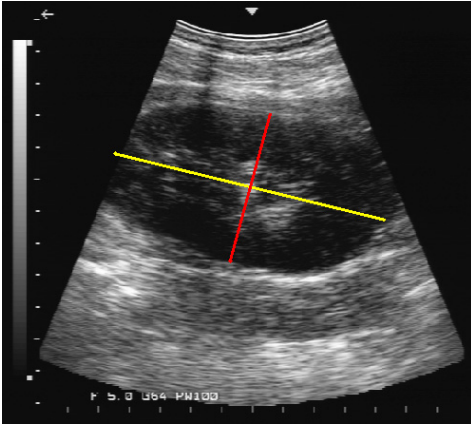


Figure 6: Localization of two ellipsoid axes for the initialization of the US segmentation. The ellipsoid axes must be placed coincident with two of the kidney axes in a central slice of the kidney. The user can rotate, move and adjust the length of the lines shown in the figure.

Using Gabor filters. The Gabor functions [47] are linear filters located in both the spatial and frequency domain. In the spatial domain, they can be decomposed into a complex sinusoid modulated by a Gaussian function, and in the frequency domain are Gaussians centered in the frequency of the sinusoid. This property of space and frequency location makes them ideal for local frequency analysis, and thus have often been used for texture analysis and feature extraction. A bank of Gabor filters with different frequencies and orientations of the sinusoid can be generated using a mother func-

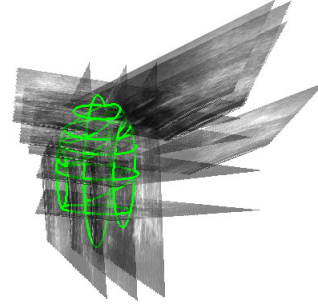


Figure 7: The initial contours for the segmentation of US images are obtained as the intersection between each image plane in 3D space and an ellipsoid defined by manual initialization.

tion. The mother function of our filter bank is:

$$G(x, y) = g(x', y') \exp(2\pi j\mathcal{F}x'), \quad (10)$$

where $(x', y') = (x \cos \theta + y \sin \theta, -x \sin \theta + y \cos \theta)$ are the coordinates rotated by angle θ , \mathcal{F} is the spacial central frequency of the function, and

$$g(x, y) = \left(\frac{1}{2\pi\sigma_x\sigma_y} \right) \exp\left(-\frac{1}{2} \left(\frac{x^2}{\sigma_x^2} + \frac{y^2}{\sigma_y^2} \right) \right) \quad (11)$$

is a Gaussian function. Since circular functions were considered, the variances of the Gaussian were $\sigma_x = \sigma_y = \sigma$. This variance σ is related to the frequency bandwidth of the Gabor filters, which in octaves is $b = \log_2[(\mathcal{F}\sigma\pi + \alpha)/(\mathcal{F}\sigma\pi - \alpha)]$, where $\alpha = \sqrt{\ln 2}/2$. We set the bandwidth of the Gabor filters to 1 octave. The central frequencies for the filter bank were selected empirically as $\mathcal{F} = \{0.08, 0.2, 0.35\}$. The frequencies were adjusted by choosing those that visually emphasize the difference between the kidney tissue and surrounding tissue in a set of training images, different from that used for testing. The usual set of angles $\theta = \{0, \pi/6, \pi/3, \pi/2, 2\pi/3, 5\pi/6\}$, covering 180° degrees, has been used.

The Gabor functions of the bank are applied to the 2D US images, and for each combination of \mathcal{F} and θ a texture feature is obtained for each image. Because Gabor functions are complex, the texture features have a real $H_{\mathcal{F},\theta}^{real}$ and an imaginary $H_{\mathcal{F},\theta}^{img}$ part. With these texture features we can define the output energy of each filter:

$$E_{\mathcal{F},\theta} = \sqrt{H_{\mathcal{F},\theta}^{real^2} + H_{\mathcal{F},\theta}^{img^2}} \quad (12)$$

These energies are normalized on the interval [0, 1] and used to control the active contours [50, 51, 35], as shown later.

Adjustment of the initial contour. As initial contour for each 2D US image, we use the ellipse obtained from the intersection between the plane of the US image located in 3D space, and the previously defined initial ellipsoid (Fig. 7). Every contour is defined by a set of points $\{P_i\}_{i=1}^{N_p}$. First, the ellipse is fit in each 2D US image using a 2D similarity transformation to better match the kidney edges. The transformation parameters are calculated finding the transformation that maximizes the integral along the ellipse of the energy gradient in the direction normal to the ellipse. The energies $E_{\mathcal{F}\theta}$ used for this computation are those corresponding to the lowest central frequency \mathcal{F}_1 . In this way, the parameter vector $p^* = [\alpha^*, s^*, t_x^*, t_y^*]$ of optimal rotation α^* , scaling s^* , and translation t^* , is obtained for each ellipse, with:

$$p^* = \operatorname{argmax}_p \sum_{n\theta=1}^{N_\theta} \sum_{i=1}^{N_p} \nabla E_{\mathcal{F}_1\theta_{n\theta}}(T(P_i; p)) \cdot \vec{N}(T(P_i; p)), \quad (13)$$

where $\nabla E_{\mathcal{F}_1\theta_{n\theta}}$ is the energy gradient corresponding to the lowest central frequency (0.08) and angle $\theta_{n\theta}$, N_θ is the number of orientations used in the Gabor filters, $\vec{N}(P_i)$ is the unit vector normal to the ellipse at point P_i , and $T(\cdot; p)$ is a similarity spatial transformation with vector of parameters p . In the maximization, only a limited number of transformations are used, among which the best is chosen. These transformations are defined by the following set of parameters: translations $t_x = \{10 \cdot n_x\}$, $t_y = \{10 \cdot n_y\}$ with $n_x = n_y = [-10, 10]$, rotations $\alpha = \{-\pi/6, 0, \pi/6\}$ and scaling $s = \{0.9, 1, 1.1\}$.

Renal medulla preprocessing. As mentioned before, it is of advantage for US renal image segmentation to eliminate the forces derived from the *renal medulla*, to avoid contours from being attracted into a local minimum. To this end, we need to detect the medulla. An image where the medulla is easier to detect can be obtained using the energies $E_{\mathcal{F},\theta}$ of the Gabor filters:

$$B = \frac{1}{N_\theta N_{\mathcal{F}}} \sum_{n_{\mathcal{F}}=1}^{N_{\mathcal{F}}} \sum_{n_\theta=1}^{N_\theta} E_{\mathcal{F}_{n_{\mathcal{F}}}, \theta_{n_\theta}} \quad (14)$$

where $N_{\mathcal{F}}$ and N_θ are the number of frequencies and orientations used in the Gabor filters, respectively. As can be seen, the B image is the mean of the resulting energies of each Gabor filter. To localize the renal medulla, this image is binarized with an empirical threshold of 0.4, obtaining B_{bin} . Next, all the z_k connected elements are searched in B_{bin} , and the ones that have no neighboring pixels outside the ellipse adjusted to the kidney are labeled as belonging to the renal medulla. This may be

expressed as:

$$M = \{z_k \in B_{bin} \mid (-L \oplus r) \cap z_k = \emptyset\}, \quad (15)$$

where M is the binary image of the medulla, L is the binary image of the ellipse adjusted to the kidney, \oplus is the morphological dilation operator and r is a 3×3 structural element. Fig. 8 shows the procedure to identify the medulla.

Active contours. In each 2D US image, the ellipse previously adjusted to the kidney is deformed using active contours. As in the 3D case, the contour is deformed by internal and external forces, and the dynamics of each vertex is given by a Newtonian law of motion (eq. 5).

The internal force is defined as:

$$\vec{F}_{int_i} = \alpha \frac{\partial^2 P_i}{\partial i^2} - \beta \frac{\partial^4 P_i}{\partial i^4} \quad (16)$$

where α and β are weights that control tension and rigidity of the curve, and $P_i = (x(i), y(i))$ is the parameterization of the curve. As in the SPECT segmentation, the external force is derived from an external force field \vec{v} . To achieve a coarse-to-fine deformation of the contour, we first deform the contour using the features obtained with the lowest central frequency and then with the higher ones. The field of forces related with each frequency \mathcal{F} is computed using the GVF algorithm [36], in order to obtain smooth external force fields without undesired local minima. To compute the edge maps $\mathcal{H}_{\mathcal{F}}$ used as input for the GVF algorithm, the energies $E_{\mathcal{F}\theta}$ are used:

$$\mathcal{H}_{\mathcal{F}} = \frac{1}{N_\theta} \sum_{n_\theta=1}^{N_\theta} \|\nabla E_{\mathcal{F}\theta_{n_\theta}}\| \quad (17)$$

In order to avoid forces created by the renal medulla edges, the image M is used to delete these edges before using the edge maps as input of the GVF algorithm. First, the zone identified as renal medulla in M (Fig. 8) is dilated with an 8×8 structural element. Then, the edges within this zone are deleted in $\mathcal{H}_{\mathcal{F}}$, and the GVF algorithm is used in the edge maps, obtaining the fields of forces. Only the normal to contour component of the force is used, as in equation (9), because the tangent component only affects the parametrization. First, the adjusted ellipse is deformed using the force field obtained with the lowest frequency Gabor filter, and then the resultant contour is deformed sequentially using the other force fields, making possible a coarse-to-fine deformation.

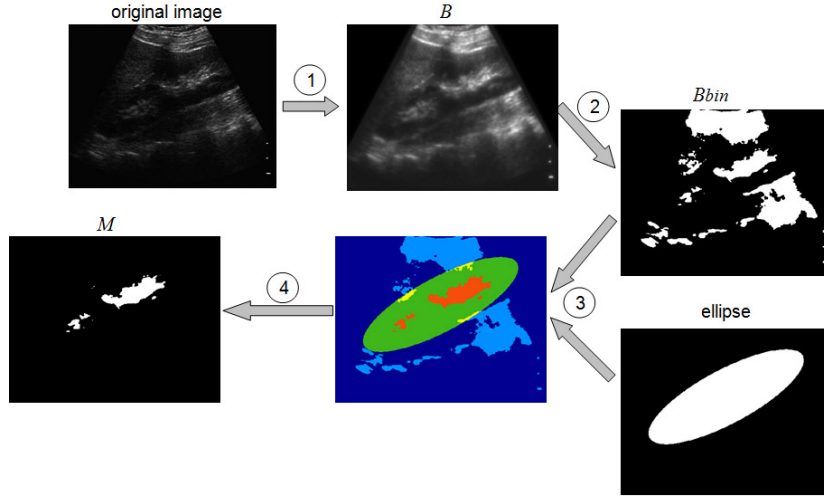


Figure 8: Renal medulla identification in the US images: 1) Computing image B as the average of the energies resulting from each Gabor filter $E_{\mathcal{F}\theta}$. 2) Binarization of image B . 3) Search the z_k connected elements (red) in B_{bin} that have no neighboring pixels outside the ellipse adjusted to the kidney. 4) Elements that represent the position of the renal medulla.

Extracting valid contours. After the deformation step, only some of the points P_i are considered as reliable. Let h_i be the value of P_i in edge map $\mathcal{H}_{\mathcal{F}}$ obtained with the highest frequency \mathcal{F} ; only the points with h_i greater than 20% of the maximal value in the curves are kept. These curve segments are joined if they are close enough (30 pixels approx.). Finally, all the small curves are eliminated, providing with highly confident border segments. Fig. 9 illustrates the final result of the whole 2.5D US segmentation process.

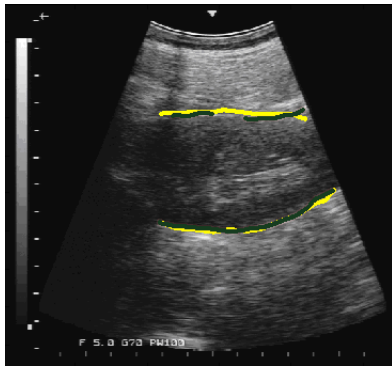


Figure 9: Superimposition of automatic (darker, green) and manual (lighter, yellow) US segmentation of the kidney contours.

2.3. Registration

The edges of the kidneys found in both images are used to perform the registration. But first, the images are per-registered to put them closer and in the same orientation. This pre-registration is based on the position

of the kidneys delivered on the initialization of the 2.5D US image segmentation (ellipsoids), and on the segmentation of the SPECT image. The centers of gravity and the main directions of these data are matched using a similarity transformation. Next, to achieve the registration, a nonlinear optimization algorithm [52] is used to minimize the quadratic distance between the points found in the 2.5D US image and the 3D kidney meshes extracted from the SPECT image. Nevertheless, as we said in the introduction, movements caused by breathing during the acquisition of the 2.5D US images, induce that the kidney position in each 2D image is slightly different. To correct this movement, the position of each US slice is adjusted iteratively together with a global registration of the entire 2.5D US image, as we show below.

We have assumed that the 3D model extracted from the SPECT image is the real shape of the kidney, therefore, the position of each US slice is adjusted using this model. In this way, the SPECT is the target image and the 2.5D US image is the floating image.

Global registration. A similarity transformation, with vector of parameters p_s (three rotation angles, three translations, and one scale parameter), is used in a global registration to minimize the distance between the edges found in both images. Thus, the minimization to find the optimal vector of parameters p_s^* is:

$$p_s^* = \operatorname{argmin}_{p_s} \sum_{c=1}^{N_c} \sum_{i=1}^{N_p(c)} d^2(T_s(P_{c,i}; p_s), S) \quad (18)$$

where, $T_s(\cdot; p_s)$ is a similarity transformation with vector of parameters p_s , N_c is the number of contours in the 2.5D US image (slices where kidney edges were detected), $N_p(c)$ is the number of points in contour c , $P_{c,i}$ is the position of point i of contour c , and $d^2(P_i, S)$ is the minimum squared distance between point P_i and the surface represented by mesh S . This minimization is performed using the Levenberg-Marquardt algorithm, which is especially suitable for minimizing functions that are a sum of squared residuals. The vector of residuals to minimize can be defined as:

$$e_s(p_s) = \left[\mathcal{E}_{1,1}(p_s), \dots, \mathcal{E}_{1,N_p(1)}(p_s), \right. \\ \left. \mathcal{E}_{2,1}(p_s), \dots, \mathcal{E}_{N_c, N_p(N_c)}(p_s) \right], \quad (19)$$

where:

$$\mathcal{E}_{c,i}(p_s) = d(T_s(P_{c,i}; p_s), S). \quad (20)$$

Thus, equation (18) can be expressed as:

$$p_s^* = \underset{p_s}{\operatorname{argmin}} \|e(p_s)\|^2, \quad (21)$$

and the vector $e_s(p_s)$ can be minimized with the Levenberg-Marquardt algorithm. To optimize the minimization, distances $d(T_s(\cdot; p_s), S)$ are pre-computed using a distance transform [53], which is also used to directly estimate the Jacobian required for the minimization algorithm. This implementation of the minimization is comparable in speed with the popular ICP (Iterative Closest Point) algorithm [54, 52]. After this distance minimization, we assume that each US slice is close enough to model S to correct movements caused by breathing using a local rigid transformation $T_r(\cdot; p_r)$.

Local registration. The distance between the contour points in the US images and S , is minimized independently for each US slice. In this way, the inconsistency in the position of some US slices, caused by movements during the 2.5D US image acquisition, can be corrected. The minimization used to find the optimal vector of parameters $p_r^*(c)$ for the rigid transformation $T_r(\cdot; p_r)$ of each contour c is:

$$p_r(c)^* = \underset{p_r}{\operatorname{argmin}} \sum_{i=1}^{N_p(c)} d^2(T_r(P_{c,i}; p_r), S). \quad (22)$$

The Levenberg-Marquardt algorithm is used again in the minimization, but in this case the vector of residuals is:

$$e_r(p_r(c)) = \left[\mathcal{E}_{c,1}(p_r(c)), \dots, \mathcal{E}_{c, N_p(c)}(p_r(c)) \right] \quad (23)$$

After the positions of all slices have been corrected, another global registration (eq. 18) is performed to improve the registration. This loop between a global registration and a local registration of each slice (Fig. 1) is repeated until the mean displacement of the points, in the registration for movement correction, is under a threshold defined as 0.5. Fig. 10 shows the 3D kidneys model and the points found in the 2.5D US image after registration. Fig. 10(a) shows the result obtained using only the global registration, and Fig. 10(b) shows the result obtained also using local registrations. An example of the final registration can be seen in Fig. 11.

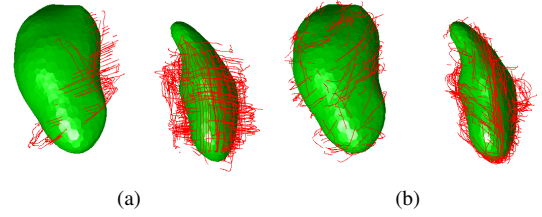


Figure 10: 3D kidneys model extracted from the SPECT image and points found in the 2.5D US image, after the registration. (a) Global registration without local registrations for movement correction. (b) Registration using local registrations for each US slice.

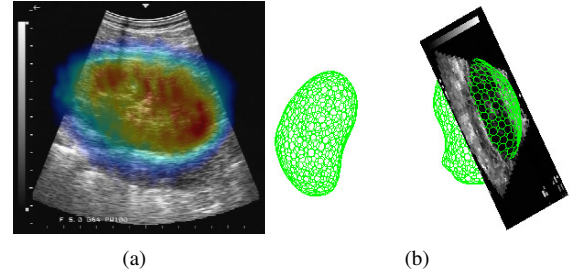


Figure 11: Example of SPECT-US image registration. a) US image superimposed with re-sliced SPECT image. b) 3D SPECT model with US image in 3D.

3. Results

3.1. SPECT Segmentation

The SPECT images were obtained injecting ^{99m}Tc -DMSA into the bloodstream, and using a dual-head gamma camera (manufacturer: SMV; model: DST-Xli). 3D images were reconstructed by applying the OSEM [55] (Ordered Subsets Expectation Maximization) iterative method, using 64 posterior projections over 180° . Image size was $128 \times 128 \times 128$ voxels, each of $4 \times 4 \times 4\text{mm}$.

Gradient and intensity SPECT segmentations were assessed on 27 exams, which were part of routine examinations ordered by physicians. Parameters used for the model dynamics were empirically calibrated over a set of training images. The parameters with better performance according to a simple visual inspection were chosen in equations (6), (7) and (9): $\gamma = 0.65$, $\lambda = 0.2$ and $\kappa = 0.8$.

The segmentations were evaluated qualitatively by a team of three medical experts using a graphic interface for visualization. As suggested in [13], the evaluation range was from 1 to 5 (1: very bad, 2: bad, 3: good, 4: very good, and 5: excellent).

For all images, the assigned score was 5. Thus, according to experts, both methods based on voxel intensity and gradient, exhibited equivalent results and are acceptable. Fig. 12 shows an example of the SPECT segmentation.

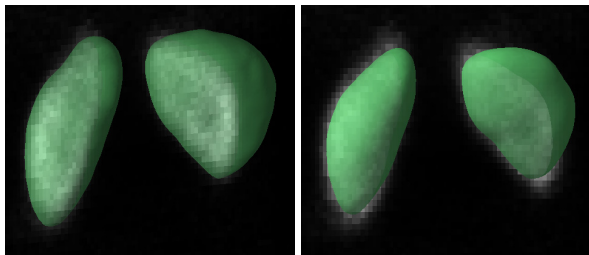


Figure 12: SPECT segmentation. Left: intensity related segmentation. Right: gradient related segmentation.

3.2. 2.5D US Segmentation

A six degrees-of-freedom optical localizer (Praxim Surgetics[®] station) was used during acquisition to determine the relative position of the 2D US slices that conform the 2.5D US image. To calibrate the system (spatial relation between the 2D images and the rigid bodies, Fig. 4) a membrane phantom method was used [56]. The US images were acquired using an echo camera *Aloka 55D-630* connected to a frame grabber. The image resolution was 480×640 with a $0.25 \times 0.19\text{mm}$ pixel size.

In order to evaluate the segmentation, seven 2.5D US exams were acquired from two patients and five healthy volunteers through posterior and lateral access. Parameters for the segmentation were chosen empirically in equations (6), (9) and (16) as: $\gamma = 0.65$, $\kappa = 10$, and $\alpha = 0.6$, $\beta = 0$. The selection criterion was the performance according to a simple visual inspection over a set of training images. The weight of the external force κ is higher than in the SPECT segmentation because in

this case the normalization was made over the energies $E_{\mathcal{F}\theta}$, and then these energies were averaged to obtain the input of the GVF algorithm. To evaluate the segmentation, the distance between our semi-automatic segmentation and a manual segmentation of the US images was measured. Medical experts participated in the manual marking of the kidneys' edges using a graphic interface specially designed for this purpose. They were asked to restrict to edges that could be clearly identified in the images. Fig. 9 shows a manual segmentation of the kidney (lighter/yellow line). Every 2.5D US image is composed of approximately 400 2D US slices. Since this number of images was large for manual evaluation, 20 images, where the kidney was visible, were randomly selected from each exam.

Table 1 shows the percentage of rejected images due to incorrect initial ellipse position, as well as average distance and percentage of borders detected in comparison to the manual segmentation. Results show that our method detect the kidney edges with a precision of approximately 3.3mm .

Table 1: Results of our US segmentation relative to manual segmentation.

Patient	Bad initialized images [%]	Edges detected [%]	Average distance [mm]
P1	5	48.85	3.64
P2	5	73.51	4.67
P3	5	58.25	3.06
P4	0	63.85	2.63
P5	10	74.57	3.84
P6	5	74.50	2.42
P7	10	65.40	2.82
Mean	5.71	65.56	3.30

3.3. Registration

The SPECT images used to validate the registration were acquired in the same set of patients and volunteers who participated in the evaluation of the 2.5D US segmentation. Two types of assessments were carried out: qualitative and quantitative. The performance of our method was compared in both assessments with a reference registration method, which uses an OL (Optical Localizer), "rigid bodies" and a spatial calibration between the SPECT and 2.5D UD acquisition systems. This registration based on an optical localizer yields good results, in [15] a RMS error of 2.03mm was obtained using a phantom and comparing the registration with direct measures of the optical localizer. However, this registration does not correct the movements caused by breathing.

Quantitative evaluation. Since the SPECT segmentation was assessed with the highest score by the medical experts, we assumed that these edges and the manual marked ones in the 2.5D US images can be used as anatomical features to evaluate the registration. Therefore, the distance between the 3D model extracted from the SPECT image and the manual US segmentation, was measured after registration. The distance was computed sampling each manual segmentation uniformly and then measuring the minimum distance between each sampled point and the surface defined by the mesh resulting from the SPECT image segmentation. Then, the average value of these distances was computed in each exam. To compare our method, the same distance was measured in a registration performed with the reference method.

Fig. 13 shows an example of the 3D SPECT segmentation overlapped with the curves of the manual US segmentation after registration. Table 2 shows the average distances obtained using the OL method, and using our method with both SPECT segmentations: gradient related segmentation (GS) and intensity related segmentation (IS). The results are of good quality, and show similar performance with both SPECT segmentations. An analysis of variance (ANOVA) was used to verify the statistical significance ($p < 0.0001$) of the difference between the results of our registration method and the OL reference one.

Table 2: Quantitative registration evaluation. Comparison between the OL (Optical Localizer) method, and our method using GS (Gradient related Segmentation) and IS (Intensity related Segmentation).

Patient	Distance [pix]		
	OL method	Our method with GS	Our method with IS
P1	2.25	1.46	1.39
P2	2.10	0.92	0.88
P3	2.07	1.29	1.15
P4	4.28	0.91	1.17
P5	2.33	1.03	0.94
P6	2.84	1.06	1.17
P7	2.49	0.84	0.79
Mean	2.62	1.07	1.07

Patient	Distance [mm]		
	OL method	Our method with GS	Our method with IS
P1	8.98	5.84	5.57
P2	8.40	3.66	3.52
P3	8.28	5.16	4.61
P4	17.11	3.65	4.68
P5	9.33	4.11	3.77
P6	11.37	4.24	4.70
P7	9.97	3.37	3.14
Mean	10.49	4.29	4.28

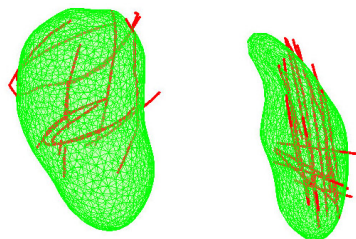


Figure 13: 3D SPECT automatic segmentation and manual US segmentation after registration. The distance between both segmentations was used as a quality measurement of the registration.

Qualitative evaluation. The registration was assessed in the same sets of US slices used in the evaluation of the 2.5D US segmentation. A group of three physicians was asked to evaluate the registration in every one of the selected US slices. The scale for the evaluation was from 1 to 5. In this scale, the score 1 was a very bad registration — images are completely out of registration and the results are not suitable for medical decisions —, and score 5 was an excellent registration — the registration is almost perfect—. Registrations with value 3 or above were considered useful for medical purposes.

The graph in Fig. 14 shows the scores obtained by the registration of the images of each patient. Table 3 shows the mean score of the OL method and our method using both, gradient and intensity related, SPECT segmentations. A “*t*-test” was used to check that the evaluation of our registration was over the clinical cut-off of 3 with $p < 0.001$, proving useful for clinical applications. Moreover, an ANOVA analysis was performed, verifying the statistical significance ($p < 0.05$) of the difference between the results of our registration method and the OL reference one.

Table 3: Qualitative registration evaluation. Comparison between the OL method and our method using GS and IS.

Type of registration	Score
OL method	3.19
Our method with GS	4.08
Our method with IS	4.13

Overall evaluation. Our method achieved better results in quantitative and qualitative evaluations, in comparison with the method based on optical localization. This improvement is because our method carries out an individual correction in the position of each US slice. The movement caused by breathing is also present during SPECT image acquisition, causing blur in the resulting image. In contrast, the 2.5D US images are not blurred

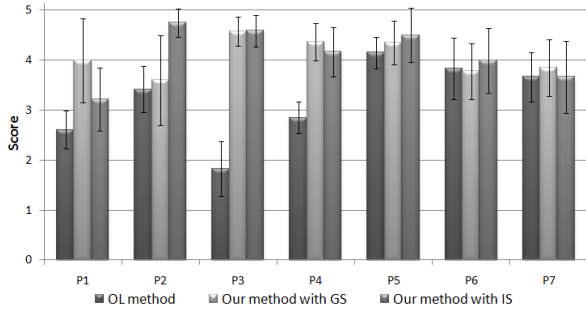


Figure 14: Scores obtained by the registrations of images of seven patients. The scores of the OL method and our method using GS and IS are showed.

because each slice is acquired independently and instantaneously. Therefore, kidney position inconsistencies may appear in the 2.5D US image if the patient moves during image acquisition, and each slice should be adjusted to match the SPECT image. Excellent results can be obtained using the method based on optical localization in slices where the position of the kidney matches the average position in the SPECT image. Nevertheless, the performance will be lower in the remaining slices. Fig. 15 shows comparisons between slices registered with our method and using an optical localizer. While in some slices the registration is very similar, in others a displacement due to patient motion can be observed.

4. Conclusion

A method has been developed in order to register renal SPECT and 2.5D US images. Usually there is not enough anatomical information in the SPECT image, which may limit its usefulness. The proposed registration makes it possible to combine functional information from the SPECT images with anatomical information from the US images. There are few studies on this type of registration in the literature, and usually they use an optical localizer and a calibration between frames of reference associated to both acquisition systems. Our method only uses information contained in the image and corrects the movement caused by patient breathing. The method is based on a previous segmentation of the images in both modalities. The SPECT segmentation, 2.5D US segmentation and the registration, were evaluated separately. The SPECT segmentation received a very good qualitative evaluation. The 2.5D US segmentation was evaluated quantitatively with a good performance and enough edges were found to guide the registration. Additionally, a method to detect the re-

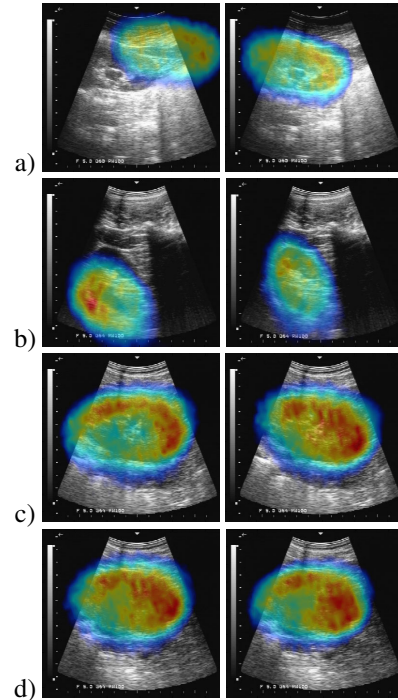


Figure 15: Left: Slices registered with the OL method. Right: Slices registered with our method. The scores obtained in the qualitative evaluation of the splices are: a)1-5 ;b)3-5 ;c)4-5 ;d)4-5

nal medulla was developed in order to improve the US segmentation. Results show that the registration was successfully performed, however, its quality could be improved. Our method take into account movements due to breathing, registering each 2D US image, but we think that important enhancement can be achieved through a better acquisition protocol to reduce kidney movements during the acquisition phase. An alternative may be to use blocked breathing during the image acquisition or to monitor the breathing to discard images that do not correspond to the same part on the respiratory cycle. From the medical point of view, it may also be useful to have an objective automatic correlation between lesions seen in the SPECT and the anatomical US image, for example, the ratio between functional lesions and volume of the kidney.

Acknowledgment

This research was partially funded by CONICYT through project FONDEF 1035, Department of Electrical Engineering and the Center for Mathematical Modelling, Universidad de Chile; and by the European project Alfa-IPECA. All exams were taken at the San

Juan de Dios hospital in Santiago, Chile. Thanks to Carmen Wriester for her help with the US images.

- [1] E. L. Kramer, J. J. Sanger, *Clinical Spect Imaging*, Raven Press. Ltd., New York, 1995.
- [2] T.-C. Yen, W.-P. Chen, S.-L. Chang, R.-S. Liu, S.-H. Yeh, C.-Y. Lin, Technetium-99m-DMSA Renal SPECT in Diagnosing and Monitoring Pediatric Acute Pyelonephritis, *The Journal of Nuclear Medicine* 37 (8) (1996) 1349–1353.
- [3] A. Gee, R. Prager, G. Treece, L. Berman, Engineering a free-hand 3D ultrasound system, *Pattern Recognition Letters* 24 (4-5) (2003) 757–777.
- [4] J. B. A. Maintz and M. A. Viergever, A survey of medical image registration, *Medical Image Analysis* 2 (1) (1998) 1–36.
- [5] T. Peters, B. Davey, P. Munger, R. Comeau, A. Evans, A. Olivier, Three-dimensional multimodal image-guidance for neurosurgery, *IEEE Trans. on Medical Imaging* 15 (2) (1996) 121–128.
- [6] R. Ellis, S. Toksvig-Larsen, M. M. D. Caramella, M. Fadda, A biocompatible fiducial marker for evaluating the accuracy of CT image registration, *Computer assisted radiology, Excerpta medica - international congress series* 1124 (1996) 693–698.
- [7] M. Fuchs, H. Wischmann, A. Neumann, J. Weese, W. Zylka, J. Sabczynski, M. H. Kuhn, T. M. Buzug, G. Schmitz, P. M. C. Gieles, Accuracy analysis for image-guided neurosurgery using fiducial skin markers, 3D CT imaging, and an optical localizer system, *Computer assisted radiology, Excerpta medica - international congress series* 1124 (1996) 770–775.
- [8] J. P. Caravel, A. François-Joubert, O. Péria, S. Dalsoglio, D. Cordonnier, P. Cinquin, Registration of anatomical and functional images of the kidney, *Medecine Nucleaire* 19 (5-6) (1995) 391–396.
- [9] B. Fei, C. Kemper, D. L. Wilson, A comparative study of warping and rigid body registration for the prostate and pelvic MR volumes, *Computerized Medical Imaging and Graphics* 27 (4) (2003) 267–281.
- [10] W. M. W. III, P. Violab, H. Atsumid, S. Nakajimae, R. Kikinis, Multi-modal volume registration by maximization of mutual information, *Medical Image Analysis* 1 (1) (1996) 35–51.
- [11] H. Zhou, T. Liu, F. Lin, Y. Pang, J. Wu, J. Wu, Towards efficient registration of medical images, *Computerized Medical Imaging and Graphics* 31 (6) (2007) 374–382.
- [12] C. Davatzikos, Nonlinear registration of brain images using deformable models, in: *Proceedings of the Workshop on Mathematical Methods in Biomedical Image Analysis (MMBIA '96)*, 94–103, 1996.
- [13] V. Walimbe, V. Zagrodsky, S. Raja, W. A. Jaber, F. P. DiFilippo, M. J. Garcia, R. C. Brunken, J. D. Thomas, R. Shekhar, Mutual information-based multimodality registration of cardiac ultrasound and SPECT images: a preliminary investigation, *Int. J. of Cardiovascular Imaging* 19 (6) (2003) 483–494.
- [14] O. Péria, L. Chevalier, A. François-Joubert, J.-P. Caravel, S. Dalsoglio, S. Lavallée, P. Cinquin, Using a 3D position sensor for registration of SPECT and US images of the kidney, in: *Computer Vision, Virtual Reality and Robotics in Medicine*, vol. 905 of LNCS, Springer Berlin / Heidelberg, 23–29, 1995.
- [15] M. Bucki, F. Chassat, F. Galdames, T. Asahi, D. Pizarro, G. Lobo, Real-Time SPECT and 2D Ultrasound Image Registration, in: *MICCAI 2007*, 219–226, 2007.
- [16] A. Leroy, P. Mozer, Y. Payan, J. Troccaz, Intensity-Based Registration of Freehand 3D Ultrasound and CT-scan Images of the Kidney, *Int. J. of Computer Assisted Radiology and Surgery* 2 (1) (2007) 31–41.
- [17] W. Wein, B. Röper, N. Navab, Integrating diagnostic B-mode ultrasonography into CT-based radiation treatment planning, *IEEE Trans. on Medical Imaging* 26 (6) (2007) 866–879.
- [18] W. Wein, S. Brunke, A. Khamene, M. R. Callstrom, N. Navab, Automatic CT-ultrasound registration for diagnostic imaging and image-guided intervention, *Medical Image Analysis* 12 (5) (2008) 577–585.
- [19] S. Gill, P. Mousavi, G. Fichtinger, E. Chen, J. Boisvert, D. Pichora, P. Abolmaesumi, Biomechanically Constrained Groupwise US to CT Registration of the Lumbar Spine, in: volume LNCS 5761, (MICCAI 2009), vol. 5761, 803–810, 2009.
- [20] E. A. Firlé, W. Chena, S. Wesarga, Registration of 3D U/S and CT images of the prostate, in: *CARS 2002 - Proceedings of the 16th International Congress and Exhibition Computer Assisted Radiology and Surgery*, 527–532, 2002.
- [21] E. A. Firlé, S. Wesarg, C. Dold, Mutual-information-based registration for ultrasound and ct datasets, *Proc. SPIE* 5370 (2004) 1130–1138.
- [22] X. Huang, J. Moore, G. Guiraudon, D. Jones, D. Bainbridge, J. Ren, T. Peters, Dynamic 2D Ultrasound and 3D CT Image Registration of the Beating Heart, *IEEE Trans. on Medical Imaging* 28 (8) (2009) 1179–1189.
- [23] A. Roche, X. Pennec, G. Malandain, N. Ayache, Rigid registration of 3-D ultrasound with MR images: a new approach combining intensity and gradient information, *IEEE Trans. on Medical Imaging* 20 (10) (2001) 1038–1049.
- [24] X. Huang, N. A. Hill, J. Ren, T. M. Peters., Rapid Registration of Multimodal Images Using a Reduced Number of Voxels, in: *Proceedings - SPIE - The International Society for Optical Engineering*, vol. 6141, 614116, 2006.
- [25] J. F. Verheya, J. Wisser, T. Keller, C.-F. Westin, R. Kikinis, Rigid overlay of volume sonography and MR image data of the female pelvic floor using a fiducial based alignment feasibility due to a case series, *Computerized Medical Imaging and Graphics* 29 (4) (2005) 243–249.
- [26] B. C. Porter, D. J. Rubens, J. G. Strang, J. Smith, S. Totterman, K. J. Parker, Three-dimensional registration and fusion of ultrasound and MRI using major vessels as fiducial markers, *IEEE Trans. on Medical Imaging* 20 (4) (2001) 354–359.
- [27] T. Lange, S. Eulenstein, M. Hünerbein, H. Lamecker, P.-M. Schlag, Augmenting intraoperative 3D ultrasound with preoperative models for navigation in liver surgery, in: *Proc. MICCAI 2004*, vol. LNCS 3217, 534–541, 2004.
- [28] G. P. Penney, J. M. Blackall, M. S. Hamady, T. Sabharwal, A. Adam, D. J. Hawkes, Registration of freehand 3D ultrasound and magnetic resonance liver images, *Medical Image Analysis* 8 (1) (2004) 81–91.
- [29] G. P. Penney, D. C. Barratt, C. S. Chan, M. Slomczykowski, T. J. Carter, P. J. Edwards, D. J. Hawkes, Cadaver Validation of Intensity-Based Ultrasound to CT Registration, in: volume LNCS 3750, (MICCAI 2005), vol. 3750, 1000–1007, 2005.
- [30] M. Baumann, P. Mozer, V. Daanen, J. Troccaz, Transrectal ultrasound prostate biopsy tracking with efficient and accurate deformation estimation, in: *IEEE International Symposium on Biomedical Imaging: From Nano to Macro*, 2009. ISBI '09, 1211–1214, 2009.
- [31] R. Shekhar, V. Zagrodsky, Mutual Information-Based Rigid and Nonrigid Registration of Ultrasound Volumes, *IEEE Trans. on Medical Imaging* 21 (1) (2002) 9–22.
- [32] C. Chan, D. Barratt, P. Edwards, G. Penney, M. Slomczykowski, T. Carter, D. Hawkes, Cadaver Validation of the Use of Ultrasound for 3D Model Instantiation of Bony Anatomy in Image Guided Orthopaedic Surgery, in: volume LNCS 3217, (MICCAI 2004), vol. 3217, 397–404, 2004.
- [33] L. Schwartz, J. Richaud, L. Buffat, E. Touboul, M. Schlienger, Kidney mobility during respiration, *Radiother Oncol.* 32 (1) (1994) 84–86.

- [34] J. M. Blackall, G. P. Penney, A. P. King, D. J. Hawkes, Alignment of Sparse Freehand 3-D Ultrasound With Preoperative Images of the Liver Using Models of Respiratory Motion and Deformation, *IEEE Trans. on Medical Imaging* 24 (11) (2005) 1405–1416.
- [35] T. McInerney, D. Terzopoulos, Deformable models in medical image analysis: A survey, *Medical Image Analysis* 1 (2) (1996) 91–108.
- [36] C. Xu, J. L. Prince, Snakes, Shapes, and Gradient Vector Flow, *IEEE Trans. on Image Processing* 7 (3) (1998) 359–369.
- [37] C. D. Garson, B. Li, S. T. Acton, J. A. Hossack, Guiding automated left ventricular chamber segmentation in cardiac imaging using the concept of conserved myocardial volume, *Computerized Medical Imaging and Graphics* 32 (4) (2008) 321–330.
- [38] W. Fang, K. L. Chan, S. Fu, S. M. Krishnan, Incorporating temporal information into active contour method for detecting heart wall boundary from echocardiographic image sequence, *Computerized Medical Imaging and Graphics* 32 (7) (2008) 590–600.
- [39] H. Delingette, General Object Reconstruction based on Simplex Meshes, *Int. J. of Computer Vision* 32 (2) (1999) 111–146.
- [40] J. Montagnat, H. Delingette, 4D deformable models with temporal constraints: application to 4D cardiac image segmentation, *Medical Image Analysis* 2 (1) (2005) 87–100.
- [41] F. J. Galdames, C. A. Pérez, P. A. Estévez, C. M. Held, Segmentation of Renal SPECT Images Based on Deformable Models, in: *SURGETICA'2005, Computer-Aided Medical Interventions: tools and applications*, Chambéry, France, 89–96, 2005.
- [42] F. J. Galdames, C. A. Pérez, P. A. Estévez, C. M. Held, F. Jaillet, G. Lobo, G. Donoso, C. Coll, Registration of Renal SPECT and 2.5D US Images, in: *SURGETICA'2007: Computer-Aided Medical Interventions: tools and applications*, Chambéry, France, 169–175, 2007.
- [43] G. M. Treece, R. W. Prager, A. H. Gee, Regularised marching tetrahedra: improved iso-surface extraction, *Computer & Graphics* 23 (4) (1999) 583–598.
- [44] M. Martín-Fernández, C. Alberola-López, An approach for contour detection of human kidneys from ultrasound images using Markov random fields and active contours, *Medical Image Analysis* 9 (2005) 1–23.
- [45] C.-H. Wu, Y.-N. Sun, Segmentation of kidney from ultrasound B-mode images with texture-based classification, *Computer Methods and Programs in Biomedicine* 84 (2) (2006) 114–123.
- [46] M. Kakar, D. R. Olsen, Automatic segmentation and recognition of lungs and lesion from CT scans of thorax, *Computerized Medical Imaging and Graphics* 33 (1) (2009) 72–82.
- [47] Y. Zhan, D. Shen, Deformable Segmentation of 3-D Ultrasound Prostate Images Using Statistical Texture Matching Method, *IEEE Trans. on Medical Imaging* 25 (3) (2006) 256–272.
- [48] J. Xie, Y. Jiang, H. Tsui, Segmentation of kidney from ultrasound images based on texture and shape priors, *IEEE Trans. on Medical Imaging* 24 (1) (2005) 45–57.
- [49] D. Shen, Y. Zhan, C. Davatzikos, Segmentation of prostate boundaries from ultrasound images using statistical shape model, *IEEE Trans. on Medical Imaging* 22 (4) (2003) 539–51.
- [50] L. D. Cohen, I. Cohen, Finite-element methods for active contour models and balloons for 2-D and 3-D images, *IEEE Trans. on PAMI* 15 (1993) 1131–1147.
- [51] M. Kass, A. Witkin, D. Terzopoulos, Snakes: Active contour models, *Int. J. of Computer Vision* 1 (4) (1987) 321–331.
- [52] A. W. Fitzgibbon, Robust registration of 2D and 3D point sets, *Image and Vision Computing* 21 (13-14) (2003) 1145–1153.
- [53] J. H. Friedman, J. L. Bentley, R. A. Finkel, An Algorithm for Finding Best Matches in Logarithmic Expected Time, *ACM Transactions on Mathematics Software* 3 (3) (1997) 209–226.
- [54] P. J. Besl, N. McKay, A method for registration of 3-D shapes, *IEEE Trans. on PAMI* 14 (2) (1992) 239–256.
- [55] M. Hudson, R. Larkin, Accelerated image reconstruction using ordered subsets of projection data, *IEEE Trans. on Medical Imaging* 13 (4) (1995) 601–609.
- [56] T. Langø, Ultrasound guided surgery: Image processing and navigation accuracy, Ph.D. thesis, Norwegian University of Science and Technology, 2000.